

Precise Control of Surface Oxygen Vacancies in ZnO Nanoparticles for Extremely High Acetone Sensing Response

Jihyun Lee

Yonsei University

Youngmoon Choi

Yonsei University

Byoung Joon Park

Pohang University of Science and Technology

Jeong Woo Han

Pohang University of Science and Technology

Hyun-Sook Lee

Yonsei University

Jong Hyeok Park

Yonsei University

Wooyoung Lee (✉ wooyoung@yonsei.ac.kr)

Yonsei University <https://orcid.org/0000-0001-8406-4324>

Research Article

Keywords: gas sensors, acetone, metal oxide semiconductors, ZnO nanoparticles, H₂O₂ treatment

Posted Date: October 6th, 2021

DOI: <https://doi.org/10.21203/rs.3.rs-948359/v1>

License: © ⓘ This work is licensed under a Creative Commons Attribution 4.0 International License.

[Read Full License](#)

Precise control of surface oxygen vacancies in ZnO nanoparticles for extremely high acetone sensing response

Jihyun Lee^{1, †}, Youngmoon Choi^{2, †}, Byoung Joon Park³, Jeong Woo Han³, Hyun-Sook Lee^{1,*}, Jong Hyeok Park^{2,*}, Wooyoung Lee^{1,*}

¹Department of Materials Science and Engineering, Yonsei University, 50 Yonsei-ro, Seodaemun-gu, Seoul, 03722, Republic of Korea

²Department of Chemical and Biological Engineering, Yonsei University, 50 Yonsei-ro, Seodaemun-gu, Seoul, 03722, Republic of Korea

³Department of Chemical Engineering, Pohang University of Science and Technology (POSTECH), Pohang, Gyeongbuk 37673, Republic of Korea

† These authors contributed equally.

*Corresponding authors: wooyoung@yonsei.ac.kr (W. Lee), lutts@yonsei.ac.kr (J. H. ark), h-slee@yonsei.ac.kr (H.-S. Lee).

Abstract

ZnO has been studied intensely for chemical sensors due to its high sensitivity and fast response. Here, we present a simple approach to precisely control oxygen vacancy contents to provide significantly enhanced acetone sensing performance of commercial ZnO nanopowders. A combination of H₂O₂ treatment and thermal annealing produces optimal surface defects with oxygen vacancies on the ZnO nanoparticles (NPs). The highest response of ~27,562 was achieved for 10 ppm acetone in 0.125 M H₂O₂ treated/annealed ZnO NPs at the optimal working temperature of 400 °C, which is significantly higher than that of reported so far in various acetone sensors based on metal-oxide-semiconductor (MOS). Furthermore, first-principles calculations indicate that pre-adsorbed O formed on the surface of H₂O₂-treated ZnO NPs can provide a favorable adsorption energy, especially for acetone detection, due to strong bidentate bonding between carbonyl C atom of acetone molecules and pre-adsorbed O on the ZnO surface. Our study demonstrates that controlling surface oxygen vacancies by H₂O₂ treatment and re-annealing at optimal temperature is an effective method to improve the sensing properties of commercial MOS materials.

Keywords: gas sensors, acetone, metal oxide semiconductors, ZnO nanoparticles, H₂O₂ treatment

1. Introduction

Monitoring environmental acetone indoor and outdoor for safety or breath acetone for non-invasive diagnosis has increased with increasing interest in health care [1]. Acetone, one of the volatile organic compounds (VOCs), is a hazardous gas that is widely used in industrial, laboratory, and domestic areas, causing indoor and outdoor environmental pollution and risking human health. Acetone with a concentration higher than 173 ppm damages not only the skin, throat, nose, and eyes but also the central nervous system [2]. The recommended occupational threshold value for acetone has been set to 250 ppm considering an 8 h time-weighted average [3]. Additionally, acetone is highly flammable owing to its high volatility even at room temperature [4]. Therefore, monitoring the acetone concentration in the environment is critical issue. Furthermore, acetone is produced in the human body through metabolic processes and released through the exhaled breath. A high concentration of breath acetone can be released due to diabetes [5], fat metabolism [6], and heart failure [7, 8]. The breath acetone concentration ranges from 0.3–0.9 ppm for healthy people [5, 6], but it is over 1.8 ppm for diabetes patients [5, 6] and over 40 ppm for a person on a ketogenic diet [6, 9]. Therefore, breath acetone can be used as a biomarker to diagnosis-related diseases such as diabetes, obesity, and systolic dysfunction.

The concentration of acetone in air or breath has been commonly measured by several techniques based on gas chromatography and mass spectrometry. These systems precisely measure the concentration; however, they are bulky, complex, time-consuming, and expensive [1]. Additionally, skilled operators are required, and gas samples must be collected before the measurement for the analysis. Resistive gas sensors based on metal-oxides semiconductors (MOS) are considered as an alternative. Among various MOS sensing materials, ZnO has been studied intensively due to its several advantages. It is chemically and thermally stable, and its various forms of nanostructure can be fabricated at a low cost. Moreover, it has favorable sensing properties such as high sensitivity and fast response.

To improve the sensing properties of ZnO, various approaches have been reported including

nanostructuring [10–12], transition metal doping [13, 14], and noble metal loading [15, 16]. Additionally, control of the surface defect [17] has been alternatively proposed because the MOS sensor response is highly dependent on the surface chemistry. The surface defect can be introduced during material synthesis [18, 19] or subsequent annealing treatment [20, 21]. Especially, oxygen vacancies, among various defects, of nanostructured ZnO play an important role in improving the sensing properties because they act as electron donors and promote the ionization and chemisorption of oxygen molecules on the ZnO surface [17, 18]. Hence, adsorbed oxygen ion species are easily generated on the surface of more oxygen-vacant ZnO, enhancing the sensing response significantly. It has been suggested that the number of oxygen vacancies of ZnO can be increased using a simple method of H₂O₂ surface treatment and annealing [22, 23]. The as-grown ZnO film and ZnO nanorods exhibited slightly enhanced sensing response compared to their untreated counterparts to detect ethanol due to the application of the surface treatment [24]. Therefore, more precisely controlled oxygen vacancy formation in ZnO is expected to be an effective strategy to improve the sensing properties of ZnO as a chemical sensor.

In this study, we found that the acetone sensing properties of commercial ZnO nanopowders were increased unprecedently via two consecutive steps; optimal H₂O₂ solution treatment and stabilized by thermal annealing. ZnO powder-based sensors which is treated by the optimal H₂O₂ concentration and high temperature annealing showed a tremendously high sensing response of more than ~27,000 to 10 ppm acetone, which is significantly higher than that reported so far for the MOS-based various acetone sensors. The sensing mechanism of the greatly enhanced response is described by the effect of surface oxygen vacancies through the analysis of surface chemistry and simulation.

2. Materials and methods

2.1 Preparation of oxygen-vacant ZnO nanoparticles

Commercial ZnO nanopowder was used to prepare the oxygen vacancies on the surface of ZnO

nanoparticles (NPs). First, 300 mg of commercial ZnO nanopowder (<50 nm, 97%, Sigma Aldrich) was dissolved into 80 mL of deionized water. Furthermore, the dissolved solution was stirred for 1 h at 75 °C. After that, 50 wt% of different concentrations of hydrogen peroxide (H₂O₂) solution (Sigma Aldrich) was poured into the mixed solution and maintained for 2 h at 75 °C under continuous stirring. The H₂O₂ aqueous solution was prepared with the following concentrations using deionized water: 0.075, 0.125, 0.25, and 1 M. The resultant white precipitate was washed with deionized water, separated by centrifugation at 11,000 rpm, and then dried at room temperature. The as-obtained ZnO₂ powders were annealed in an air atmosphere for 2 h at 400 °C for transforming it into an oxygen-deficient ZnO nanopowder with a pale yellow color.

2.2 Characterization of sensing materials

The crystal structures and morphology of the prepared powders were characterized by X-ray diffraction (XRD, Ultima IV, Rigaku) with Cu K α radiation (1.5406 Å) and high-resolution transmission electron microscopy (HR-TEM, JEM-ARM 200F, JEOL), respectively. The chemical states of the sample surface were investigated using X-ray photoelectron spectroscopy (XPS, K-alpha, Thermo Scientific Incorp.) with Al K α source (1486.6 eV). Moreover, the XPS results were calibrated by adventitious carbon C 1s peak at 285 eV. Raman spectra were measured by Horiba Jobin Yvon HR800 UV with Ar⁺ laser excitation of 488 nm to understand chemical states further.

2.3 Fabrication of sensor devices

Interdigitated Pt electrodes were patterned on a SiO₂/Si substrate (8.5 mm × 8.5 mm) using photolithographic technique after depositing Pt layer (100 nm) using a DC magnetic sputtering system to fabricate the sensor devices. The Cr layer (20 nm) was deposited to provide good adhesion Pt layer and the substrate. The as-prepared nanopowders were mixed with an α -terpineol binder; the mixtures were spread on the interdigitated Pt electrodes. The sensor device was annealed at 600 °C in a nitrogen environment for 1h to remove the binding agent and enhance the stability of

the sensor.

2.4 Gas sensing measurements

The sensing performance of the H₂O₂ treated and annealed ZnO NPs for acetone was tested with a customized sensing measurement system. The sensor device was mounted on a chamber of tube furnace equipped with a gas flow system connected with mass flow controllers (MFCs) and gas cylinders. Furthermore, the acetone concentration was controlled by adjusting the flow rate between the high concentration of acetone and synthetic air of a balance gas. The adjusted amount of acetone and synthetic air was injected into the sensor chamber at 100 sccm of a constant flow rate. The operating temperature of the sensor was controlled using a temperature controller of the tube furnace. The sensing performance of the samples was examined in the temperature range of 300–500 °C. Moreover, the electric sensing response of the samples was measured using a nanovoltmeter (Keithley 2182) at 10 nA of a constant current with a time interval of 1 s using a current source (Keithley 6220). The sensing response was defined as $\Delta R/R_g$, where $\Delta R = R_a - R_g$. R_a and R_g represent the resistance in air and acetone gas, respectively.

2.5 Computational details

We performed first-principles calculations considering spin-polarized density functional theory using the Vienna ab initio Simulation Package [25, 26] and projected augmented wave (PAW) potentials [27, 28]. Perdew-Burke-Ernzerhof (PBE) functional using the generalized gradient approximation (GGA) was considered for electronic exchange and correlation [29]. All calculations used a plane-wave basis set with a cutoff of 500 eV. The convergence threshold for total energy calculations was set at 10^{-4} eV. All geometry optimizations were conducted using a conjugate gradient algorithm considering the forces acting on each atom and terminated when they converged within 0.03 eV/Å for electronic relaxation. The k -point sampling of the Brillouin zone was used with a $3 \times 3 \times 1$ Monkhorst-Pack grid [30]. We obtained the bulk ZnO parameters: $a = b = 3.289$ Å

and $c = 5.307 \text{ \AA}$, which agree very well with the previous experimental data ($a = b = 3.250 \text{ \AA}$ and $c = 5.207 \text{ \AA}$) [31]. The slab models representing the $\text{ZnO}(10\bar{1}0)$ surface consisted of three ZnO double-layers separated by approximately 18 \AA vacuum regions. In all cases, the atoms in the bottom ZnO double layer were fixed for simulating the underlying bulk structure. The calculations for gas-phase molecules were performed in a $20 \text{ \AA} \times 21 \text{ \AA} \times 22 \text{ \AA}$ supercell.

3. Results and discussion

To characterize the crystal structure modification of the commercial ZnO nanoparticles (NPs) by the H_2O_2 treatment and the subsequent thermal annealing, XRD measurements were conducted as shown in Figure 1(a). It shows the XRD patterns of 1) pure ZnO NPs, 2) ZnO NPs after 1 M H_2O_2 treatment and 3) ZnO NPs after 1 M H_2O_2 treatment followed by thermal annealing. The ZnO NPs with a hexagonal wurtzite structure (JCPDS No. 36-1451) were easily transformed into the ZnO_2 cubic phase (JCPDS No. 76-1364) after 1 M H_2O_2 treatment due to the reaction in Equation (1) (see Figure 1(a)) [24]. The diffraction peaks of the annealed samples after 1 M H_2O_2 treatment were well-indexed to the crystal structure of the ZnO phase without any impurities and secondary phases. However, it releases oxygen by thermal decomposition at a temperature above $200 \text{ }^\circ\text{C}$ and easily converts to a more stable phase, ZnO, at high temperatures (Equation (2)) [24]. Particularly, oxygen vacancies were formed on the surface of ZnO during its transformation from ZnO_2 to ZnO [24].



The XRD results indicated that the crystal structure of the ZnO NPs changed to cubic ZnO_2 phase during H_2O_2 treatment and returned to the hexagonal ZnO phase after annealing at $400 \text{ }^\circ\text{C}$. Hence, the surface of ZnO particles was damaged presumably during the H_2O_2 treatment and re-annealing step, forming surface defects. The surface defect was observed by TEM. Figures 1(b) and 1(d) show the high-resolution TEM image of ZnO NP and 0.125 M H_2O_2 treated/annealed ZnO NPs,

respectively. Both images show the clear lattice fringes with an interplanar spacing of approximately 0.28 nm, ascribing to the (100) plane in the hexagonal ZnO. The surface of ZnO NP had clear lattice fringes; however, the surface of the 0.125 M H₂O₂ treated/annealed ZnO NP had more damaged (see the magnified TEM images of Figures 1(c) and 1(e), respectively).

We prepared various ZnO NPs that were annealed at 400 °C after H₂O₂ treatments with different molar concentrations (*x* M) to investigate the effect of H₂O₂ on the sensing performance of the final ZnO product. The crystalline phase of these NPs was compared to that of pure ZnO. Figure 2(a) shows the XRD spectra of the pure ZnO and *x* M H₂O₂ treated/annealed ZnO (*x* = 0.075, 0.125, 0.250, and 1.000) NPs. All the prepared NPs had the hexagonal ZnO phase. However, the overall diffraction peak intensity decreases with increasing H₂O₂ concentration, *x* (Figures 2(a) and 2(b)). The intensity of the main peak (*) was compared with that of the pure ZnO NPs. As shown in Figure 2(c), the peak intensity slightly decreases at the 0.125 M compared to pure ZnO; however, it is abruptly decreased at the 0.250 M. Additionally, the sharp diffraction peaks broadened from 0.250 M (Figure 2(b)), which means a significant decrease in crystallinity at the concentrations of H₂O₂ over 0.250 M. We found from the broadening of the diffraction peaks that the particle size decreases for H₂O₂ concentrations above 0.250 M.

We calculated the crystallite size of the as-prepared nanopowders using the Halder-Wagner method as follows:

$$\left(\frac{\beta \cdot \cos\theta}{\sin\theta}\right)^2 = \frac{K\lambda}{D} \frac{\beta}{\tan\theta \cdot \sin\theta} + 16\varepsilon^2, \quad (3)$$

where *D* represents the crystallite size, *β* denotes the peak width at half-maximum intensity, *K* is the crystallite configuration constant, *λ* is the wavelength of Cu K_α radiation, and *ε* denotes the weighted average strain [32]. The crystallite size can be determined from the slope of (β/tanθ)² versus β/(tanθ·sinθ) plot [33]. The Halder-Wagner plots for all prepared samples after adopting the *K* = 4/3 for the volume-weighted average size of spherical crystallites [33] are shown in Figures 3(a)–(e). The calculated crystallite sizes are summarized in Figure 3(f). The size of commercial

ZnO NPs and 0.075 and 0.125 M treated/annealed ZnO NPs was in the range of 52–55 nm. It was significantly reduced to ~19 and ~11 nm for 0.250 and 1.000 M treated/annealed ZnO NPs, respectively. These outcomes are in good agreement with the results obtained from the TEM analysis provided in Figures 4(a)–(e).

The sensing performance of the pure ZnO NPs was measured after exposing them to acetone at different concentrations (0.01–10 ppm) at different operating temperatures (300–500 °C). Figure 5(a) shows a representative plot of variation in sensing responses of the 0.125 M H₂O₂ treated/annealed ZnO NPs to 10 ppm of acetone at different operating temperatures. Figure 5(b) presents maximum sensing response of the pure ZnO NPs and *x* M H₂O₂ treated/annealed ZnO NPs (*x* = 0.075, 0.125, 0.250, and 1.000) as a function of operating temperature. All the samples show their highest response at 400 °C, implying an optimal operating temperature. Particularly, the highest response for 10 ppm acetone was observed to be ~27,562 from the sample of 0.125 M H₂O₂ treated/annealed ZnO NPs. Additionally, the 0.125 M H₂O₂ treated/annealed ZnO NPs show a fast response time in the range of 1.3–2.6 s at various working temperatures of 300–500 °C (see the inset of Figure 5(a)).

The response time was estimated using a definition—the time required to reach 90% of the total change in response. Figure 5(c) shows the variation in sensing response of the 0.125 M H₂O₂ treated/annealed ZnO NPs to different acetone concentrations (0.01–10 ppm) at the optimal operating temperature of 400 °C. The result indicates that the sample can detect ultra-low concentration of 0.01 ppm acetone. Figure 5(d) shows the maximum response as a function of acetone concentration. The response has a good linear relationship with acetone concentration (linear correlation coefficient, $R^2 = 0.989$). The sensitivity of the 0.125 M H₂O₂ treated/annealed ZnO NPs for detecting acetone in the range of 0.01–10 ppm was estimated to be approximately 2,725 via a slope obtained by linear fitting.

According to the sensing results, the 0.125 M H₂O₂ treated/annealed ZnO NPs exhibited extremely high sensing response for the detection of 10 ppm acetone among the prepared samples.

Because the sensing performances are strongly influenced by the chemical states of the metal oxide surface we performed surface elemental composition analysis by XPS. The chemical states of the sample surface were analyzed by probing the Zn 2p and O 1s states. Figure 6(a) shows the XPS spectra of the Zn 2p state for all samples. All samples show two main peaks corresponding to the electronic states of Zn 2p_{1/2} (~1044 eV) and Zn 2p_{3/2} (~1021 eV), indicating the existence of a divalent oxidation state of Zn atoms in ZnO crystals. Furthermore, we observed that the Zn 2p_{3/2} spectra peak was shifted to the lower binding energy for 0.075 and 0.125 M treated/annealed ZnO NPs, as seen in Figure 6(b). Additionally, more shift was observed for the 0.125 M samples. The shift of Zn 2p_{3/2} peak to lower binding energy is closely related to the existence of oxygen vacancies in ZnO. The binding energies of Zn 2p_{3/2} in ZnO were decreased with an increasing concentration of oxygen vacancies [34].

The existence of oxygen vacancies in the as-prepared ZnO NPs was analyzed by the detailed characterization of the O 1s state in XPS spectra. Figure 6(c)–(g) shows that the O 1s peaks are deconvoluted into three distinct Gaussian peaks centered at ~530, ~531, and ~532 eV. These peaks are associated with O²⁻ ions of Zn-O bonds in the ZnO wurtzite (O-lattice), the adsorbed oxygen ions, O⁻ and O²⁻, in the oxygen-deficient regions within ZnO (O-deficient), and the chemisorbed oxygen species, such as adsorbed O₂ and H₂O on the surface of ZnO (O-chemisorbed), respectively [35]. Among the three different types of oxygen states, the O-deficient state is considered to be directly related to the sensing performance [36]. The number of oxygen vacancies was estimated by calculating the relative percentage of the area fraction of the O-deficient peak. The percentage of oxygen vacancies of the commercial ZnO NPs was ~36% (see Figure 6(c)). Furthermore, oxygen vacancies of the H₂O₂ treated/annealed ZnO NPs for various concentrations are as follows: ~41% for 0.075 M, ~46% for 0.125 M, ~38 for 0.250 M, and ~37% for 1.000 M. According to the XRD analysis, 0.250 and 1.000 M samples had the smaller particles than the rest. Therefore, a larger number of oxygen vacancies is expected due to their higher surface-to-volume ratio. However, that was not the case (see Figures 6(f) and 6(g)) due to the reduced ZnO phase formation, as revealed in

Figure 2. Particularly, the 0.075 and 0.125 M samples had higher contents of oxygen vacancies than the other two. Specifically, the 0.125 M sample had more vacancies than the 0.075 M sample. Therefore, the shift of XPS Zn 2p_{3/2} peak to lower energy in the 0.075 and 0.125 M samples is undoubtedly attributed to the increased oxygen vacancy.

The analysis of Raman spectra was performed to confirm the existence of oxygen vacancies further. Figure 7 shows the Raman spectra of the commercial ZnO NPs and that of 0.075, 0.125, and 0.250 M H₂O₂ treated/annealed ZnO NPs. Four Raman modes were observed at 331, 381, 440, and 584 cm⁻¹, associated with the ZnO wurtzite structure [37, 38]. The sharp and strong peak at 440 cm⁻¹ can be assigned to the nonpolar optical phonon E_2^{high} mode [39]. The small peaks around 331 and 381 cm⁻¹ can be attributed to $E_2^{high} - E_2^{low}$ multiphonon scattering phonon mode and A_1^{TO} transverse optical phonon mode, respectively. The polar phonon peaks centered at 584 cm⁻¹ is A_1^{LO} longitudinal optical phonon mode, which is attributed to defects such as oxygen vacancies [40]. The Raman spectra were normalized with respect to the $E_2^{high} - E_2^{low}$ peak for ease of interpretation (see Figure 8). The ratio between A_1^{LO} and E_2^{high} peak intensities ($I(A_1^{LO})/I(E_2^{high})$) indicates the number of oxygen vacancies in the sample [37, 38]. The contents of oxygen vacancies increase in the 0.125 M sample but decrease in the 0.250 M samples (see inset of Figure 7). This trend is consistent with the results obtained from the XPS analysis, as shown in Figure 6(c)–(g).

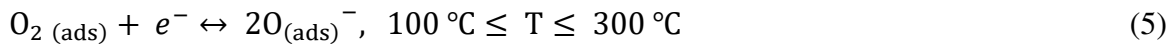
We compared the sensing responses of all the prepared samples upon exposure to 10 ppm acetone at the optimal working temperature of 400 °C (see Figure 8). The response was ~1,070 for commercial ZnO NPs, ~7,359 for 0.075 M, ~27,562 for 0.125 M, ~3,068 for 0.250 M, and ~1,807 for 1.000M H₂O₂ treated/annealed ZnO NPs. The relative percentage of the number of oxygen vacancies obtained from the XPS O 1s peak analysis is also shown in Figure 6(c)–(g). The sensing response of the samples shows the same trend as that of the number of oxygen vacancies. Oxygen vacancies in the ZnO surface are considered to be adsorption sites of oxygen species for sensing reaction and then, acetone molecules react to the adsorbed oxygen species on the ZnO surface. We

also confirmed that the ZnO surface covered with oxygen species is more preferred for the adsorption of acetone molecules thermodynamically. This result was obtained from computational calculations, and we discuss more about it in the later section. Therefore, a higher sensing response can be explained by the increased number of oxygen vacancies. The H₂O₂ treated/annealed ZnO NPs show a highly improved sensing response than the commercial ZnO NPs, as shown in Figure 8. In particular, the 0.125 M sample displays the best sensing response. The results reveal that the H₂O₂ treatment and annealing process can easily produce oxygen vacancies on the surface of ZnO NPs. The optimal concentration of H₂O₂ for the best acetone sensing response of ZnO NPs was found to be approximately 0.125 M. Additionally, the highest sensing response value of ~27,562 for acetone 10 ppm is remarkably higher than that of previously reported various acetone sensors based on metal oxide semiconductors [41–53], as shown in Figure 9. This indicates that controlling the number of oxygen vacancies by H₂O₂ treatment is a very effective way to improve the sensing performance using simply commercial NPs.

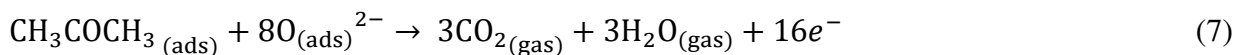
Furthermore, we tested other sensing properties, such as sensitivity for other target gases and repeatability for the detection of acetone, of the 0.125 M H₂O₂ treated/annealed ZnO NPs at its optimal working temperature of 400 °C. Figure 10(a) shows the response of the sample to various gases, such as acetone, dimethyl methylphosphonate (DMMP), hydrogen sulfide, ethanol, toluene, isoprene, benzene, formaldehyde, methane, hydrogen, CO, and CO₂, at the same concentration of 10 ppm at 400 °C. The response to acetone was remarkably high than that of the other gases, indicating that the sensor based on the 0.125 M H₂O₂ treated/annealed ZnO NPs provides a clear distinction during acetone gas detection. Figure 10(b) shows the repeatability of the 0.125 M H₂O₂ treated/annealed ZnO NPs during sensing measurement for the detection of 10 ppm acetone over 60 cycles at 400 °C. Furthermore, Figure 10(c) shows the magnified plot of the real-time resistance curves marked by the dotted box in Figure 10(b). Figures 10(b) and (c) clearly show that the sensing resistance is approximately constant throughout the 60 cycles of continuous detection of 10 ppm acetone. This implies the good repeatability in the response of the 0.125 M H₂O₂ treated/annealed

ZnO NPs for sensing 10 ppm acetone.

A possible mechanism for the pristine ZnO and oxygen-vacant ZnO NPs for the detection of acetone based on the characterization results of surface chemistry is illustrated in Figure 11. The mechanism is based on the change in the electrical resistance of ZnO during adsorption and desorption of gas molecules on the ZnO surface. When the ZnO NPs are under ambient air, the O₂ molecules in the air are adsorbed on the surface of ZnO NPs, and the adsorbed O₂ molecules take the electrons from the conduction band of the ZnO (Figure 11(a), left). Subsequently, O²⁻ ions are formed on the ZnO surface at the optimal operating temperature of 400 °C in the air (Figure 11(a), left). Different types of oxygen ion species, such as O₂⁻, O⁻, or O²⁻, are formed depending on the working temperature based on Equations (4)–(6) [54]:



These reactions show that an electron depletion layer is formed on the surface of ZnO, resulting in high resistance of the sample (Figure 11(a), left). When the sample is exposed to acetone (CH₃COCH₃) gas, the gas molecules react with the adsorbed oxygen ion species (O²⁻). Many electrons are released back to the ZnO conduction band (Figure 11(a), right), as shown by Equation (7) [19]. Subsequently, the thickness of the depletion layer decreases, resulting in a decrease in the resistance (Figure 11(a), right). These resistance change, before and after the chemical reaction of the target gas molecules with oxygen ion species on the sample surface, corresponds to the sensing response.



The oxygen vacancies act as acceptors of oxygen ion species in the air at high temperatures in the case of oxygen-vacant ZnO NPs through H₂O₂ treatment and annealing [29]. Many oxygen ion species are adsorbed, and the thicker depletion layer is generated (Figure 11(b), left). Therefore, the

resistance of oxygen-vacant ZnO NPs in the air become higher than that of untreated ones. Then the adsorbed acetone molecules interact with a greater number of oxygen ion species during the sensing reaction, leading to a significant decrease in resistance. Accordingly, the oxygen-vacant sample exhibited a significantly sensitive and improved acetone gas sensing response.

We further performed density functional theory calculations to elucidate the high sensing response of H₂O₂ treated/annealed ZnO NPs for acetone. The non-polar ZnO(10 $\bar{1}$ 0) surface was used as the slab model because it is not only the most stable surface of ZnO [55, 56], but also the dominating surface as verified from our XRD results. We constructed the oxygen full-covered ZnO(10 $\bar{1}$ 0) surface and calculated the adsorption energies of acetone, ethanol, and methane on it to describe the oxygen-adsorbed ZnO surface in gas molecule sensing conditions. The adsorption energies of acetone, ethanol, and methane were calculated using the following equation:

$$\Delta E_{\text{ads}} = E_{\text{molecule+slab}} - (E_{\text{slab}} + E_{\text{molecule}}), \quad (7)$$

where ΔE_{ads} denotes the adsorption energy, $E_{\text{molecule+slab}}$ represents the total energy of surface and adsorbed molecule, E_{slab} is the total energy of the surface, and E_{molecule} denotes the total energy of an isolated molecule. The optimized adsorption configurations of acetone, ethanol, and methane on the oxygen full-covered ZnO(10 $\bar{1}$ 0) surface are depicted in Figure 12(a), and their adsorption energies are plotted in Figure 12(b). The adsorption energies reveal that ethanol (-0.35 eV) and methane (-0.03 eV) can be considered as weak physisorption; however, acetone is most strongly adsorbed on the ZnO surface (-1.47 eV). In the adsorption configuration of acetone, pre-adsorbed oxygen (dark-red) of ZnO surface binds to carbonyl C atom of acetone when carbonyl O atom (red) of acetone binds to Zn atom at the surface. This bidentate adsorption configuration is thermodynamically favorable for acetone on the oxygen full-covered ZnO(10 $\bar{1}$ 0) surface, compared to other weakly physisorbed molecules.

Additionally, we calculated the adsorption energies on the ZnO surface with the different content of pre-adsorbed oxygen—clean surface, one oxygen atom-adsorbed surface, and full

oxygen-covered surface— to explain the effect of pre-adsorbed oxygen on the adsorption strength at the ZnO surface. The results of the calculation are presented in Figure 12(c). Ethanol (-1.00 eV) has stronger adsorption than acetone (-0.58 eV) on a clean ZnO surface (orange bar). In this case, ethanol forms not only the bonds between hydroxyl O atom and surface Zn atom but also hydrogen bonding between hydroxyl H atom and lattice O atom. However, acetone (-1.31 eV) binds more strongly on the ZnO surface in one oxygen-adsorbed ZnO surface (blue bar) with bidentate configuration bonding between carbonyl C of acetone and pre-adsorbed O on the ZnO surface. This difference in adsorption configuration between the clean and oxygen pre-adsorbed surfaces of acetone makes it more favorable to be adsorbed on the ZnO surface with pre-adsorbed oxygen. In the case of methane adsorption, all ZnO surfaces show the weak physisorption of methane. Acetone is most favorable to be bound on the ZnO surface with pre-adsorbed oxygen among the three gas molecules due to adsorption energies on different ZnO surfaces.

The surface of oxygen-vacant ZnO NPs can be covered with the large number of oxygen ion species, as mentioned in the sensing mechanism part of Figure 11. Therefore, highly enhanced sensing response of 0.125 M H₂O₂ treated/annealed ZnO NPs than that of bare ZnO NPs (Figure 8) is attributed to the higher adsorption energy of acetone molecules, especially in the oxygen full-covered ZnO surface due to the bidentate configuration bonding between carbonyl C of acetone and pre-adsorbed O on the ZnO surface, as described by the simulation (Figure 12(c)). Furthermore, the remarkably high response of the 0.125 M H₂O₂ treated/annealed ZnO NPs to acetone than other gases, such as ethanol and methane (Figure 10(a)), is explained by significantly higher adsorption energies of acetone than ethanol and methane (see Figure 12 (b)).

4. Conclusion

We show that only a simple H₂O₂ treatment and annealing process can significantly improve the acetone sensing performance of commercial ZnO NPs by creating abundant oxygen vacancies on

the surface of ZnO NPs. The ZnO NPs, annealed after surface treatment with an optimized H₂O₂ content of 0.125 M, exhibited a significantly higher sensing response of ~27,562 to 10 ppm acetone at the optimal working temperature of 400 °C than untreated commercial ZnO NPs. Moreover, this value is remarkably higher than that reported so far for various acetone sensors based on MOS. The surface defect of oxygen vacancies was verified by analyzing surface chemistry using XPS and Raman spectroscopy. Therefore, the significantly high response of the 0.125 M sample can be attributed to the generation of many oxygen vacancies on the surface of ZnO NPs. Consequently, we developed a highly sensitive acetone sensor based on ZnO with a simple surface treatment. In addition, first-principles calculations indicate that pre-adsorbed O formed on the surface of H₂O₂-treated ZnO NPs can provide a favorable adsorption energy, especially for acetone detection, due to strong bidentate bonding between carbonyl C atom of acetone molecules and pre-adsorbed O on the ZnO surface. Our study demonstrates that the control of surface oxygen vacancies by H₂O₂ treatment is an effective method to improve the sensing response significantly. Furthermore, the surface treatment method can be adopted to other commercial MOS NPs without the complicated material synthesis process, reducing the manufacturing time of sensor devices and enabling large-scale fabrication.

Acknowledgments

This research was supported by the Basic Science Research Program (2017M3A9F1052297) and the Priority Research Centers Program (2019R1A6A1A11055660) through the National Research Foundation of Korea (NRF), funded by the Korean government (Ministry of Science and ICT) and the Technology Innovation Program ('20013621', Center for Super Critical Material Industrial Technology) funded by the Ministry of Trade, Industry & Energy (MOTIE, Korea). H.-S. Lee thanks the Basic Research in Science and Engineering Program of NRF (2021R1A2C1013690).

References

- [1] V. Amiri, H. Roshan, A. Mirzaei, G. Neri, A. I. Ayesh, Nanostructured Metal Oxide-Based Acetone Gas Sensors: A Review, *Sensors* 20 (2020) 3096.
- [2] Q. Jia, H. Ji, Y. Zhang, Y. Chen, X. Sun, Z. Jin, Rapid and selective detection of acetone using hierarchical ZnO gas sensor for hazardous odor markers application, *J. Hazard. Mater.* 276 (2014) 262–270.
- [3] M. Šetka, F. A. Bahos, D. Matatagui, I. Gràcia, E. Figueras, J. Drbohlavová, S. Vallejos, Love Wave Sensors with Silver Modified Polypyrrole Nanoparticles for VOCs Monitoring, *Sensors* 20 (2020) 1432.
- [4] J.-S. Do, S.-H. Wang, On the sensitivity of conductimetric acetone gas sensor based on polypyrrole and polyaniline conducting polymers, *Sens. Actuators, B Chem.* 185 (2013) 39–46.
- [5] C. Deng, J. Zhang, X. Yu, W. Zhang, X. Zhang, Determination of acetone in human breath by gas chromatography–mass spectrometry and solid-phase microextraction with on-fiber derivatization, *J. Chromatogr. B* 810 (2004) 269–275.
- [6] G. Neri, A. Bonavita, G. Micali, N. Donato, Design and development of a breath acetone MOS sensor for ketogenic diet control, *IEEE Sens. J.* 10 (2010) 131.
- [7] M. Kupari, J. Lommi, M. Ventila, U. Karjalainen, Breath acetone in congestive heart failure, *Am. J. Cardiol.* 76 (1995) 1076.
- [8] F. G. Marcondes-Braga, I. G. R. Cutz, G. L. Batista, P. H. N. Saldiva, S. M. Ayub-Ferreira, V. S. Issa, S. Mangini, E. A. Bocchi, F. Bacal, Exhaled acetone as a new biomarker of heart failure severity, *Chest* 142 (2012) 457.
- [9] J.C. Anderson, Measuring breath acetone for monitoring fat loss: review, *Obesity* 23 (2015) 2327.
- [10] T.-R. Rashid, D.-T. Phan, G.-S. Chung, A flexible hydrogen sensor based on Pd nanoparticles decorated ZnO nanorods grown on polyimide tape, *Sens. Actuators B: Chem.* 185 (2013) 777–784.

- [11] X. Yu, F. Song, B. Zhai, C. Zheng, Y. Wang, Electro spun ZnO nanotubes and its gas sensing applications, *Phys. E: Low-Dimens. Syst. Nanostruct.* 52 (2013) 92–96.
- [12] S. B. Khan, M. Faisal, M. M. Rahman, A. Jamal, Low-temperature growth of ZnO nanoparticles: photocatalyst and acetone sensor, *Talanta* 85 (2011) 943–949.
- [13] N. H. Al-Hardana, M. J. Abdullah, A. Abdul Aziz, Performance of Cr-doped ZnO for acetone sensing, *Appl. Surf. Sci.* 270 (480) (2013) 485.
- [14] M. H. Darvishnejad, A. A. Firooz, J. Beheshtian, A. A. Khodadadi, Highly sensitive and selective ethanol and acetone gas sensors by adding some dopants (Mn, Fe, Co, Ni) onto hexagonal ZnO plates, *RSC Adv.* 6 (2016) 7838–7845.
- [15] L. Wang, S. Wang, M. Xu, X. Hu, H. Zhang, Y. Wang, W. Huang, A Au-functionalized ZnO nanowire gas sensor for detection of benzene and toluene, *Phys. Chem. Chem. Phys.* 15 (2013) 17179–17186.
- [16] A. Koo, R. Yoo, S. P. Woo, H.-S. Lee, W. Lee, Enhanced acetone-sensing properties of Pt-decorated Al-doped ZnO nanoparticles, *Sens. Actuators, B Chem.* 280 (2019) 109–119.
- [17] L. Zhu, W. Zeng, Room-temperature gas sensing of ZnO-based gas sensor: A review, *Sensors and Actuators A* 267 (2017) 242–261
- [18] L. Zhanga, Y. Yin, Large-scale synthesis of flower-like ZnO nanorods via a wet-chemical route and the defect-enhanced ethanol-sensing properties, *Sens. Actuators, B Chem.* 183 (2013) 110–116.
- [19] L. Zhang, J. Zhao, H. Lu, L. Gong, L. Li, J. Zheng, H. Li, Z. Zhu, High sensitive and selective formaldehyde sensors based on nanoparticle-assembled ZnO microoctahedrons synthesized by homogeneous precipitation method, *Sens. Actuators, B Chem.* 160 (2011) 364–370.
- [20] M. Chen, Z. Wang, D. Han, F. Gu, G. Guo, Porous ZnO polygonal nanoflakes: synthesis, use in high-sensitivity NO₂ gas sensor, and proposed mechanism of gas sensing, *J. Phys. Chem. C* 115 (2011) 12763–12773.
- [21] M.W. Ahn, K.S. Park, J.H. Heo, J.G. Park, D.W. Kim, K.J. Choi, J.H. Lee, S.H. Hong, Gas

- sensing properties of defect-controlled ZnO-nanowire gas sensor, *Appl. Phys. Lett* 93 (2008) 263103.
- [22] J. Wang, Z. Wang, B. Huang, Y. Ma, Y. Liu, X. Qin, X. Zhang, Y. Dai, Oxygen Vacancy Induced Band-Gap Narrowing and Enhanced Visible Light Photocatalytic Activity of ZnO, *ACS Appl. Mater. Interfaces* 4 (2012) 4024–4030.
- [23] X. Li, J. Song, Y. Liu, H. Zeng, Controlling oxygen vacancies and properties of ZnO, *Curr. Appl. Phys.* 14 (2014) 521–527.
- [24] W. Kim, M. Choi, K. Yong, Generation of oxygen vacancies in ZnO nanorods/films and their effects on gas sensing properties, *Sens. Actuators B Chem.* 209 (2015) 989–996.
- [25] G. Kresse and J. Hafner, *Ab initio* molecular dynamics for liquid metals, *Phys. Rev. B* 47 (1993) 558–561.
- [26] G. Kresse and J. Furthmüller, Efficient iterative schemes for *ab initio* total-energy calculations using a plane-wave basis set, *Phys. Rev. B* 54 (1996) 11169–11186.
- [27] P.E. Blöchl, Projector augmented-wave method, *Phys. Rev. B* 50 (1994) 17953–17979.
- [28] G. Kresse and D. Joubert, From ultrasoft pseudopotentials to the projector augmented-wave method, *Phys. Rev. B* 59 (1999) 1758–1775.
- [29] J.P. Perdew, K. Burke, and M. Ernzerhof, Generalized Gradient Approximation Made Simple, *Phys. Rev. Lett.* 77 (1996) 3865–3868.
- [30] H.J. Monkhorst and J.D. Pack, Special points for Brillouin-zone integrations, *Phys. Rev. B* 13 (1976) 5188–5192.
- [31] S.C. Abrahams and J.L. Bernstein, Remeasurement of the structure of hexagonal ZnO, *Acta Cryst.* 25 (1969) 1233–1236.
- [32] N.C. Halder, C.N.J. Wagner, Separation of particle size and lattice strain in integral breadth measurements, *Acta Cryst.* 20 (1966) 312–313.

- [33] T. Ida, S. Shimazaki, H. Hibino, H. Toraya, Diffraction peak profiles from spherical crystallites with lognormal size distribution, *J. Appl. Crystallogr.* 36 (2003) 1107–1115.
- [34] Z. Geng, X. Kong, W. Chen, H. Su, Y. Liu, F. Cai, G. Wang, J. Zeng, Oxygen Vacancies in ZnO Nanosheets Enhance CO₂ Electrochemical Reduction to CO, *Angew. Chem. Int. Ed.* 57 (2018) 6054–6059.
- [35] J. Wang, Y. Li, Y. Kong, J. Zhou, J. Wu, X. Wu, W. Qin, Z. Jiao, L. Jiang, Nonfluorinated superhydrophobic and micro/nano hierarchical Al doped ZnO film: the effect of Al doping on morphological and hydrophobic properties, *RSC Adv.* 5 (2015) 81024–81029.
- [36] J. Gan, X. Lu, J. Wu, S. Xie, T. Zhai, M. Yu, Z. Zhang, Y. Mao, S.C.I. Wang, Y. Shen, Y. Tong, Oxygen Vacancies Promoting Photoelectrochemical Performance of In₂O₃ Nanocubes, *Sci. Rep.* 3 (2012) 1021.
- [37] A. Momot, M. N. Amini, G. Reekmans, D. Lamoen, B. Partoens, D. R. Slocombe, K. Elen, P. Adriaensens, A. Hardy, M. K. Van Bael, A novel explanation for the increased conductivity in annealed Al-doped ZnO: an insight into migration of aluminum and displacement of zinc, *Phys. Chem. Chem. Phys.* 19 (2017) 27866–27877.
- [38] V. Russo, M. Ghidelli, P. Gondoni, C. S. Casari and A. Li Bassi, Multi-wavelength Raman scattering of nanostructured Al-doped zinc oxide, *J. Appl. Phys.* 115 (2014) 073508.
- [39] Y. Yang, C. Wang, B. Wang, Z. Li, J. Chen, D. Chen, N. Xu, G. Yang, and J. Xu, Radial ZnO nanowire nucleation on amorphous carbons, *Appl. Phys. Lett.* 87 (2005) 183109.
- [40] L. Yang, Y. Tang, A. Hu, X. Chen, K. Liang, and L. Zhang, Raman scattering and luminescence study on arrays of ZnO doped with Tb³⁺, *Physica B* 403 (2008) 2230–2234.
- [41] J. Huang, Y. Wu, C. Gu, M. Zhai, K. Yu, M. Yang, J. Liu, Large-scale synthesis of flowerlike ZnO nanostructure by a simple chemical solution route and its gas-sensing property, *Sens. Actuators B Chem.* 146 (2010) 206–212
- [42] B. L. Zhu, C. S. Xie, W. Y. Wang, K. J. Huang, J. H. Hu, Improvement in gas sensitivity of ZnO thick film to volatile organic compounds (VOCs) by adding TiO₂, *Mater. Lett.* 58 (2004)

- [43] K.-W. Kim, P.-S. Cho, S.-J. Kim, J.-H. Lee, C.-Y. Kang, J.-S. Kim, S.-J. Yoon, The selective detection of C₂H₅OH using SnO₂-ZnO thin film gas sensors prepared by combinatorial solution deposition, *Sens. Actuators B Chem.* 123 (2007) 318–324
- [44] L. Qin, J. Xu, X. Dong, Q. Pan, Z. Cheng, Q. Xiang, F. Li, The template-free synthesis of square-shaped SnO₂ nanowires: The temperature effect and acetone gas sensors, *J. Nanosci. Nanotechnol.* 19 (2008) 185705
- [45] J. Shin, S.-J. Choi, I. Lee, D.-Y. Youn, C.O. Park, J.-H. Lee, H.L. Tuller, I.-D. Kim, Thin-wall assembled SnO₂ fibers functionalized by catalytic Pt nanoparticles and their superior exhaled-breath-sensing properties for the diagnosis of diabetes, *Adv. Funct. Mater.* 23 (2013) 2357–2367.
- [46] J. Xu, Y. Li, H. Huang, Y. Zhu, Z. Wang, Z. Xie, X. Wang, D. Chen, G. Shen, Synthesis, characterizations and improved gas-sensing performance of SnO₂ nanospike arrays, *J. Mater. Chem. A.*, 21 (2011) 19086–19092.
- [47] J. Huang, X. Xu, C. Gu, M. Yang, M. Yang, J. Liu, Large-scale synthesis of hydrated tungsten oxide 3D architectures by a simple chemical solution route and their gas-sensing properties, *J. Mater. Chem. A.* 21 (2011) 13283–13289.
- [48] M. Righettoni, A. Tricoli, S.E. Pratsinis, Si:WO₃ sensors for highly selective detection of acetone for easy diagnosis of diabetes by breath analysis, *Analytical Chemistry*, 82 (2010) 3581–3587.
- [49] C.-Y. Lee, C.-M. Chiang, Y.-H. Wang, R.-H. Ma, A self-heating gas sensor with integrated NiO thin-film for formaldehyde detection, *Sens. Actuators B Chem.* 122 (2007) 503–510.
- [50] R. Rella, J. Spadavecchia, M.G. Manera, S. Capone, A. Taurino, M. Martino, A.P. Caricato, T. Tunno, Acetone and ethanol solid-state gas sensors based on TiO₂ nanoparticles thin film deposited by matrix assisted pulsed laser evaporation, *Sens. Actuators B Chem.* 127 (2007)

426–431.

- [51] S.-J. Choi, I. Lee, B.-H. Jang, D.-Y. Youn, W.-H. Ryu, C.O. Park, I.-D. Kim, Selective diagnosis of diabetes using Pt-functionalized WO₃ hemitube networks as a sensing layer of acetone in exhaled breath, *anal. chem.*, 85 (2013) 1792–1796.
- [52] S. Zhu, X. Liu, Z. Chen, C. Liu, C. Feng, J. Gu, Q. Liu, D. Zhang, Synthesis of Cu-doped WO₃ materials with photonic structures for high performance sensors, *J. Mater. Chem. A.* 20 (2010) 9126–9132.
- [53] A.K. Nayak, R. Ghosh, S. Santra, P.K. Guha, D. Pradhan, Hierarchical nanostructured WO₃-SnO₂ for selective sensing of volatile organic compounds, *Nanoscale* 7 (2015) 12460-12473.
- [54] Z. Ahmad, A.Z. Sadek, K. Latham, J. Kita, R. Moos, W. Wlodarski, Chemically synthesized one-dimensional zinc oxide nanorods for ethanol sensing. *Sens. Actuators B: Chem.* 187 (2013) 295–300..
- [55] C. Wöll, The chemistry and physics of zinc oxide surfaces. *Prog. Surf. Sci.* 82 (2007) 55–120.
- [56] J. Goclon and B. Meyer, The interaction of H₂S with the ZnO(10 $\bar{1}$ 0) surface. *Phys. Chem. Chem. Phys.* 15 (2013) 8373–8382.

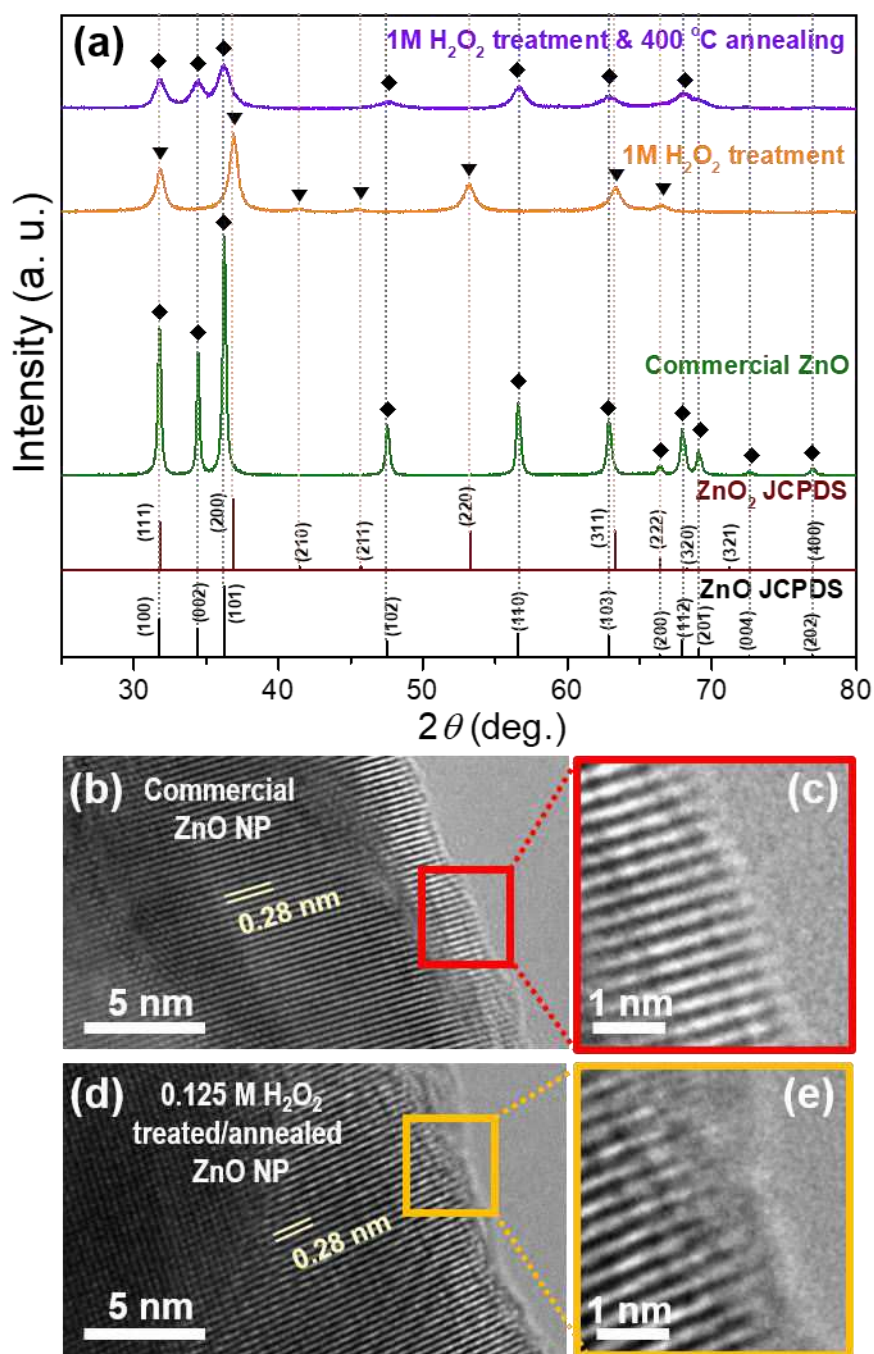


Figure 1. (a) XRD patterns of commercial ZnO, 1 M H₂O₂ treated ZnO, and 1 M H₂O₂ treated/annealed ZnO. The standard XRD patterns of hexagonal wurtzite ZnO (JCPDS No. 36-1451) and cubic ZnO₂ (JCPDS No. 76-1364) are shown as vertical lines at the bottom. High-resolution TEM image of (b), (c) commercial ZnO NP and (d), (e) 0.125 M H₂O₂ treated/annealed ZnO NP.

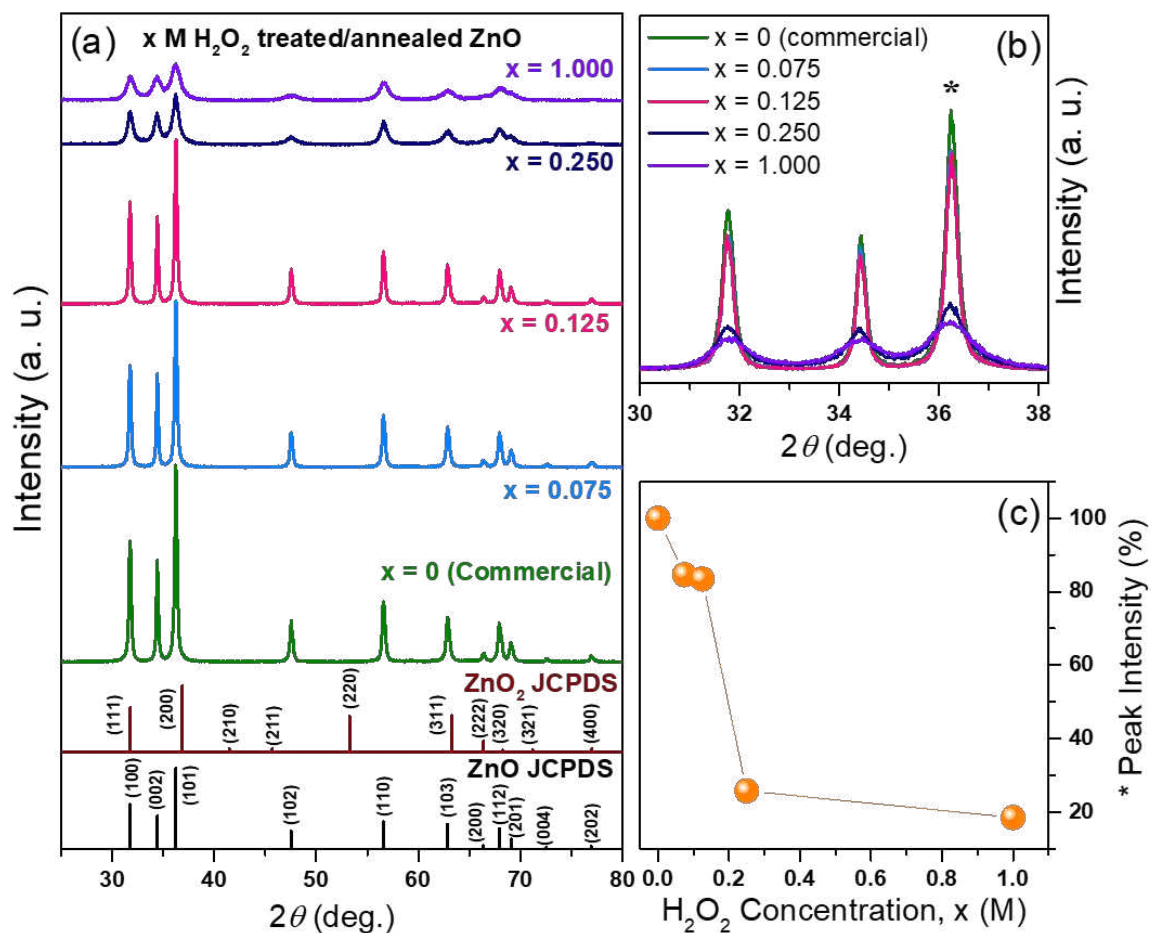


Figure 2. (a) XRD patterns of commercial ZnO and x M H₂O₂ treated/annealed ZnO ($x = 0.075$, 0.125 , 0.25 , and 1) nanopowders. (b) Magnified three main peaks of the prepared ZnO samples. (c) The intensity of the first main peak (*) as a function of H₂O₂ concentration.

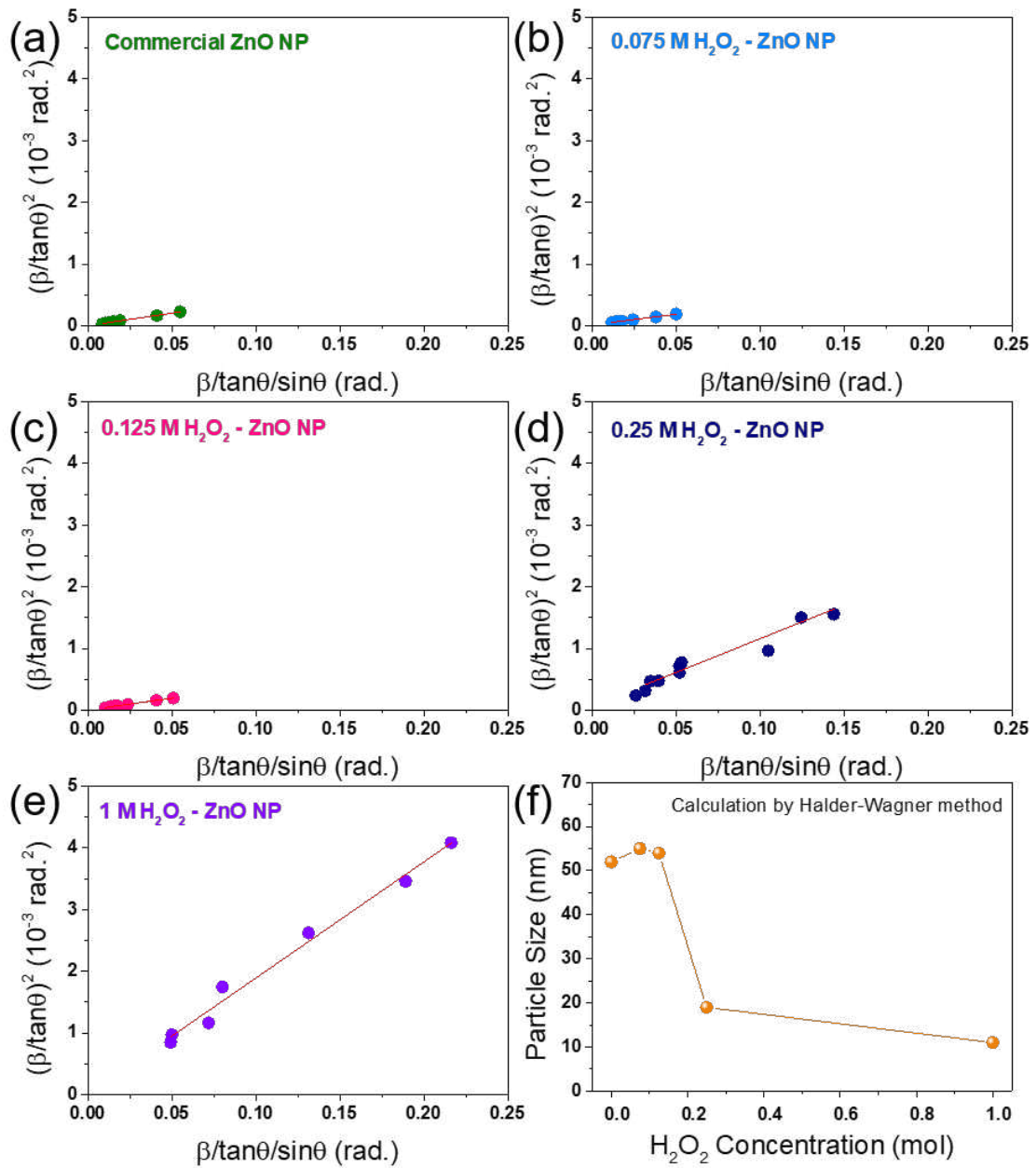


Figure 3. Halder-Wagner plots of (a) commercial ZnO NPs, (b) 0.075M H_2O_2 treated/annealed ZnO, (c) 0.125 M H_2O_2 treated/annealed ZnO NPs, (d) 0.25 M H_2O_2 treated/annealed ZnO NPs, and (e) 1M H_2O_2 treated/annealed ZnO NPs. (f) Crystalline size estimated from the slope of the linear fit.

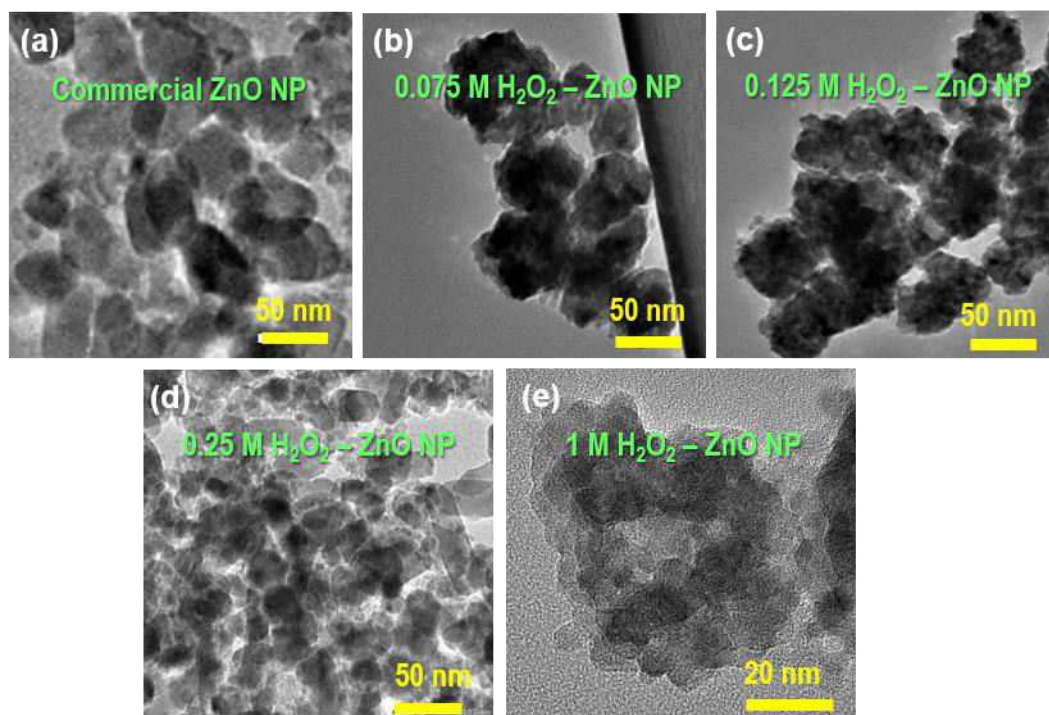


Figure 4. TEM images of (a) commercial ZnO NPs, (b) 0.075M H₂O₂ treated/annealed ZnO, (c) 0.125 M H₂O₂ treated/annealed ZnO NPs, and (d) 0.25 M H₂O₂ treated/annealed ZnO NPs.

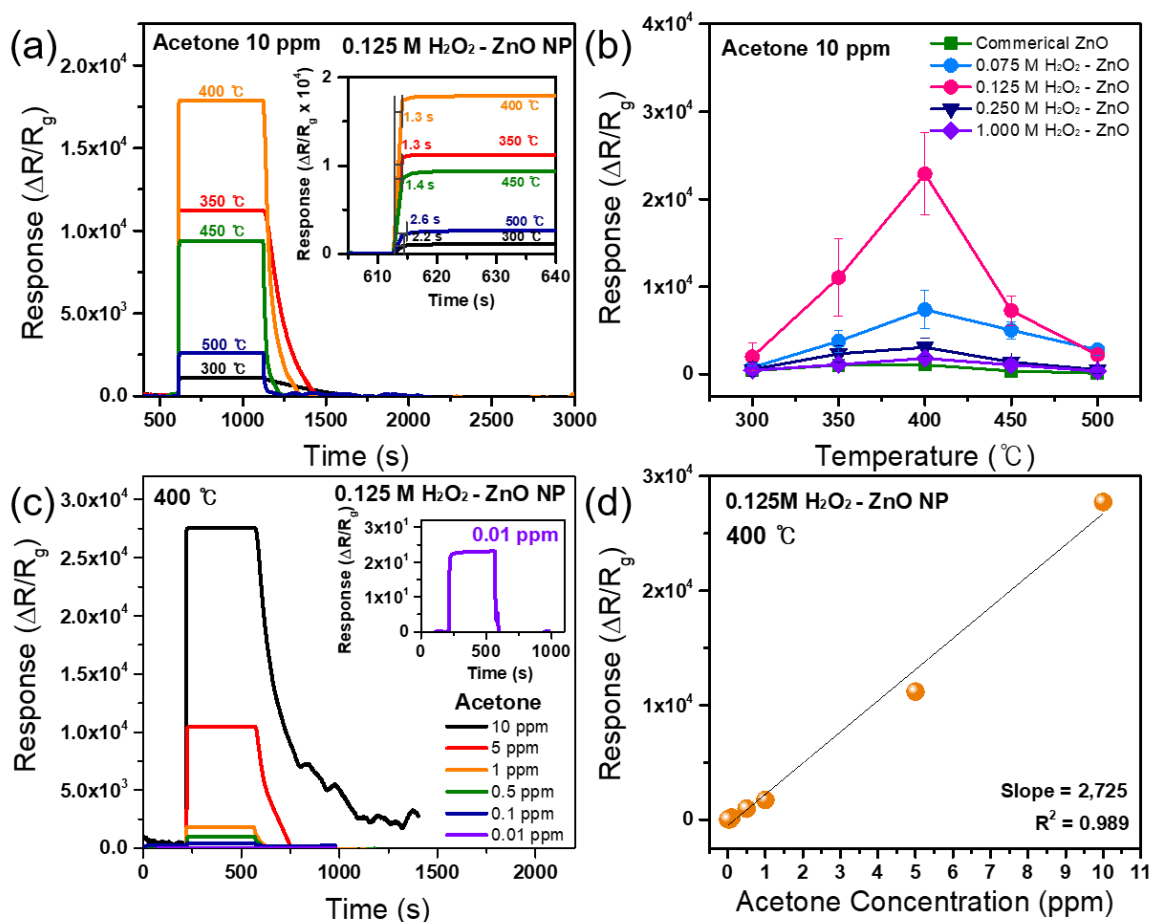


Figure 5. (a) Variation in the response of 0.125 M H_2O_2 treated/annealed ZnO NPs to 10 ppm acetone in the operating temperature range of 300–500 °C. Inset depicts response times from their sensing curves. (b) Maximum sensing response of the commercial ZnO NPs and x M H_2O_2 treated/annealed ZnO NPs ($x = 0.075, 0.125, 0.25,$ and 1) at 10 ppm acetone as a function of operating temperature. (c) Variation in the response of the 0.125 M sample at an optimum operating temperature (400 °C) as a function of acetone concentration. (d) Sensing response of 0.125 M sample to different concentrations of acetone in the range of 0.1–10 ppm at 400 °C. Sensitivity was calculated from a slope of a linear fit of the response.

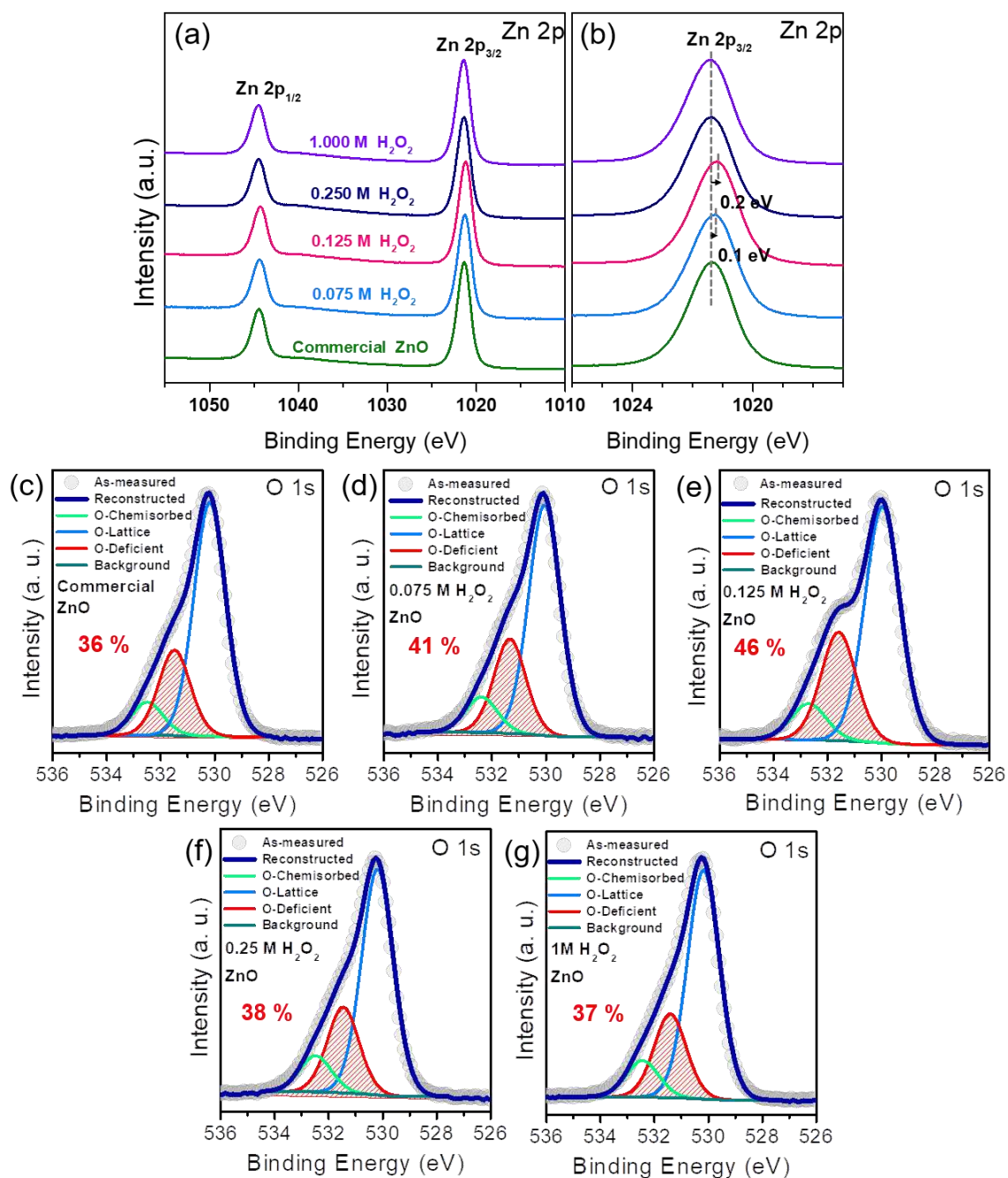


Figure 6. (a) Zn 2p XPS spectra of commercial ZnO NPs and x M H₂O₂ treated/annealed ZnO NPs ($x = 0.075, 0.125, 0.250,$ and 1.000); (b) Zn 2p_{3/2} peak of the samples; (c)–(g) O 1s XPS spectra of (c) commercial ZnO NPs and x M H₂O₂ treated/annealed ZnO NPs ($x =$ (d) 0.075, (e) 0.125, (f) 0.250, and (g) 1.000).

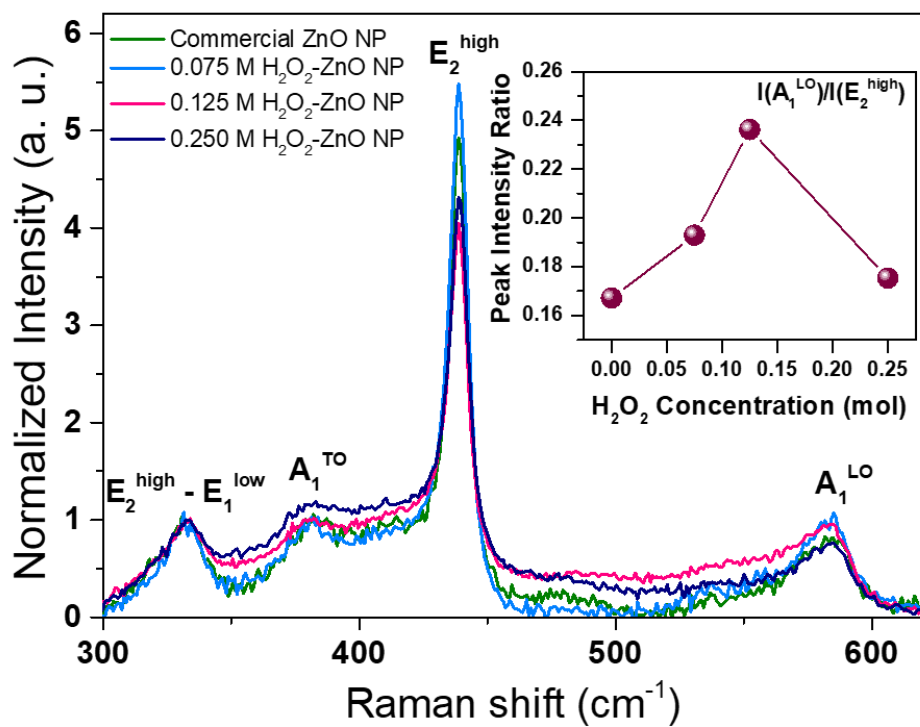


Figure 7. Raman spectra of commercial ZnO NPs and x M H₂O₂ treated/annealed ZnO NPs ($x = 0.075, 0.125, \text{ and } 0.25$).

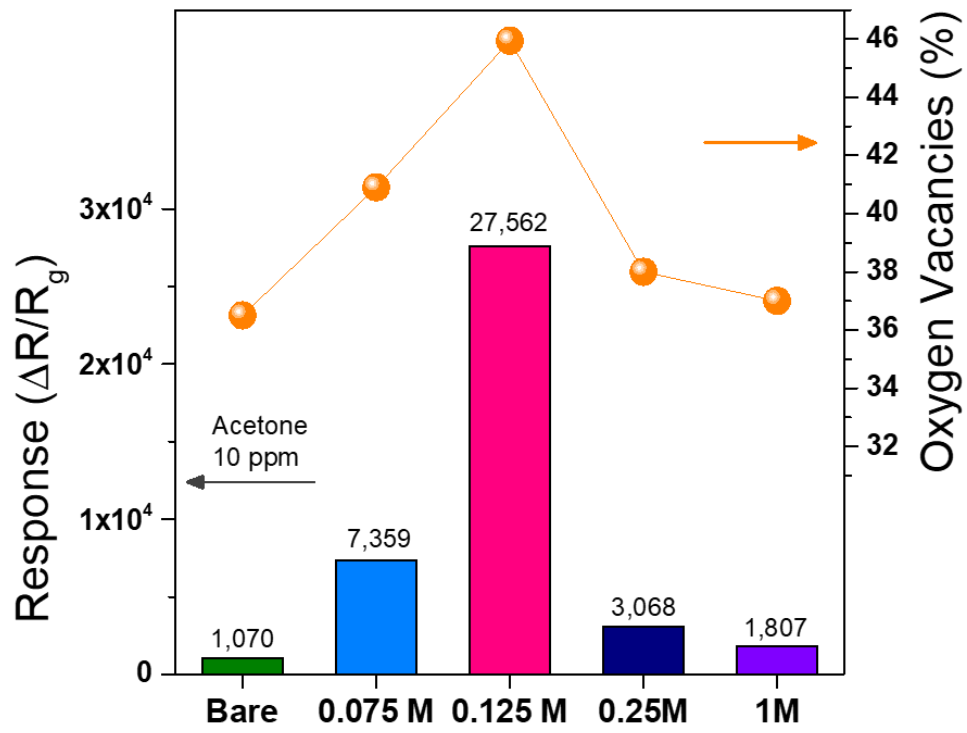


Figure 8. Overall comparison of responses and fraction of oxygen vacancies.

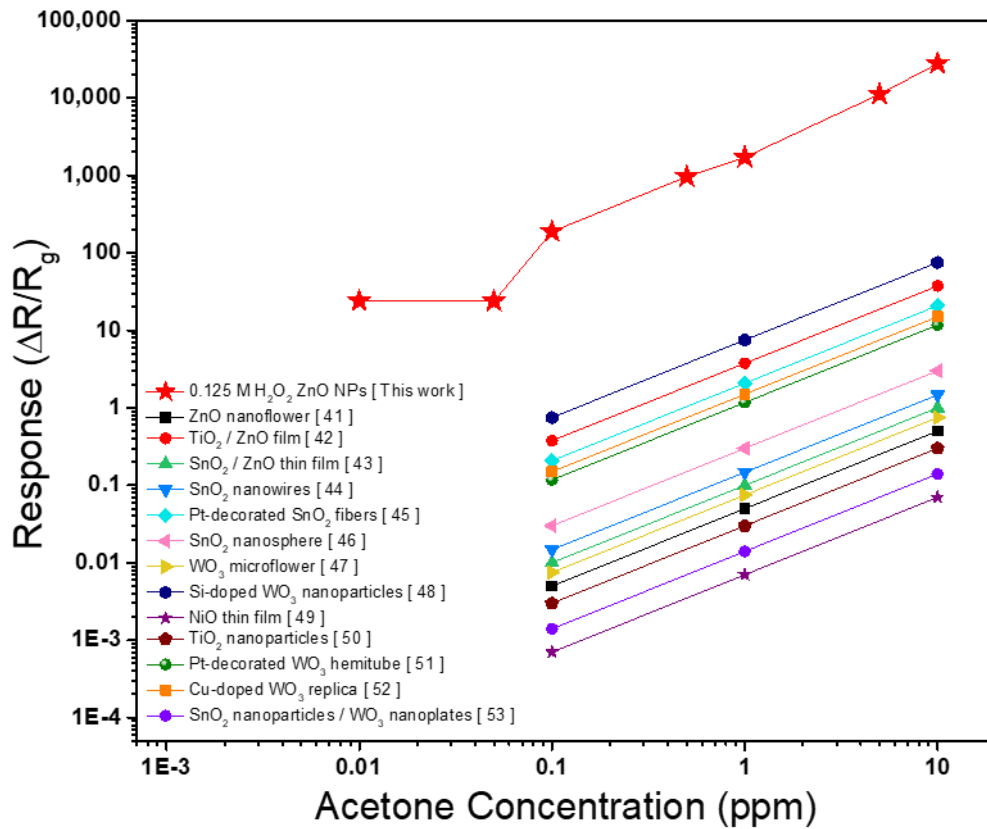


Figure 9. Comparison of sensing response of 0.125 M H₂O₂ treated/annealed ZnO NPs to previously reported metal-oxide semiconductor-based gas sensors for various concentrations of acetone.

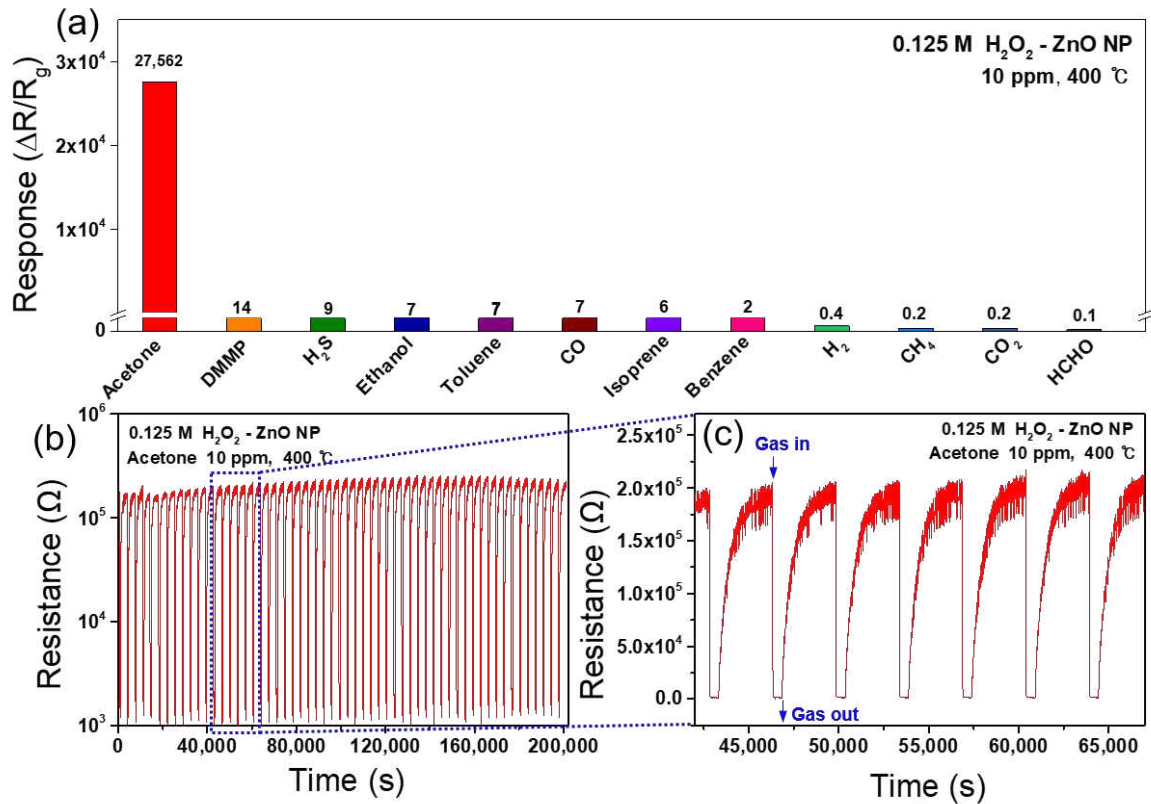


Figure 10. (a) Sensing response of the 0.125 M H_2O_2 treated/annealed ZnO NPs to various gases, such as acetone, dimethyl methylphosphonate (DMMP), H_2S , ethanol, toluene, CO, isoprene, benzene, H_2 , CH_4 , CO_2 , and HCHO, at the same concentration of 10 ppm at the optimal working temperature of 400 °C. (b) Reliability of 0.125 M sample for detecting 10 ppm acetone over 60 cycles at 400 °C; (c) magnified plot of the real-time resistance curves marked by a box in (b).

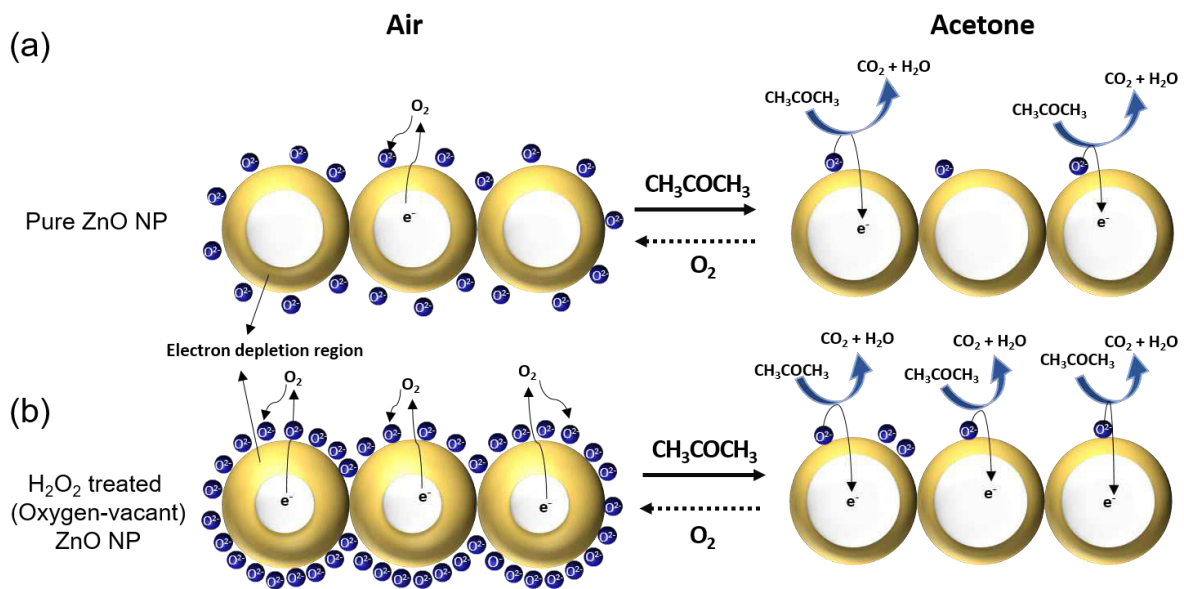


Figure 11. Schematic illustration of the sensing reaction mechanism of (a) commercial ZnO NPs and (b) H_2O_2 treated/annealed (oxygen-vacant) ZnO NPs in air and acetone.

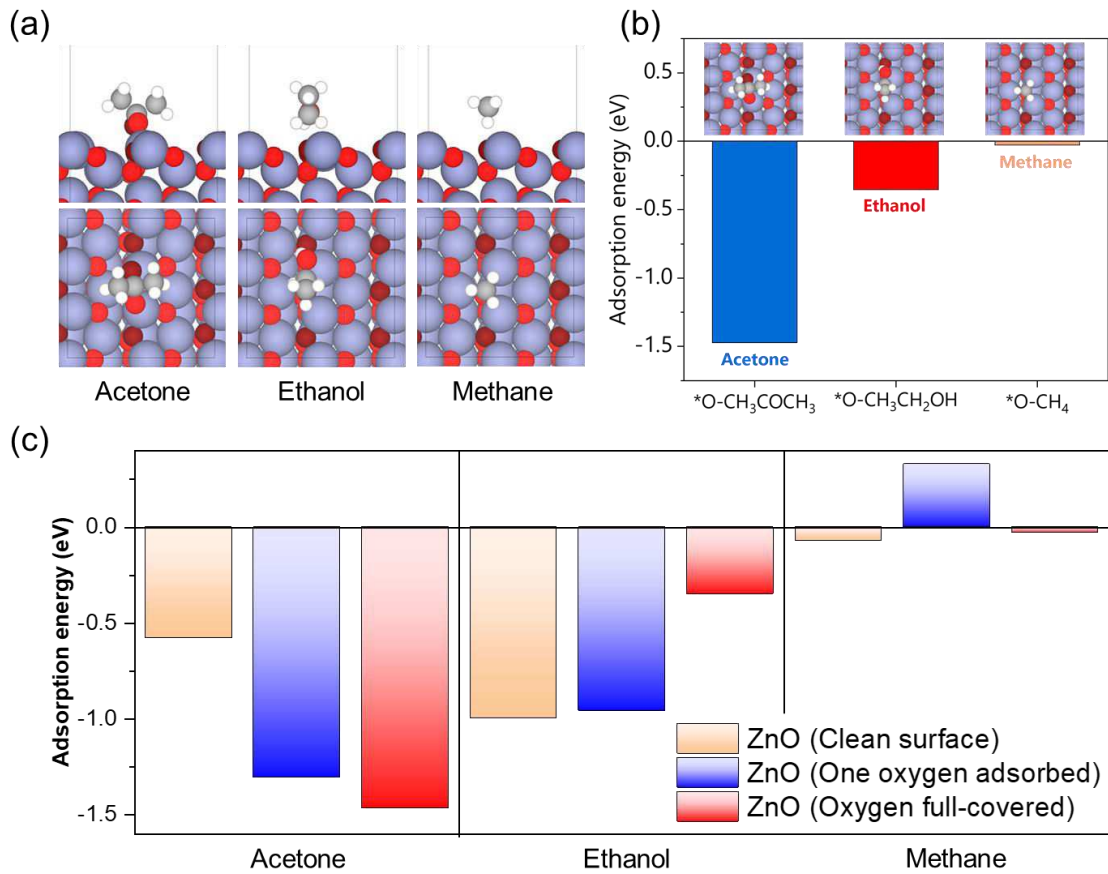


Figure 12. (a) The optimal adsorption configurations of acetone, ethanol, and methane on oxygen ion species full-covered ZnO[1010] surface in the cross section view (upper panel) and the top section view (lower panel). (b) Plot of adsorption energy (ΔE_{ads}) corresponding to each configuration of (a). Here, ΔE_{ads} was obtained by $\Delta E_{\text{ads}} = E_{\text{molecule+slab}} - (E_{\text{slab}} + E_{\text{molecule}})$. (c) ΔE_{ads} plot of each gas molecules on the ZnO according to the various surface condition; clean surface, one oxygen adsorbed surface, and oxygen full-covered surface.